



**HAL**  
open science

## A new Monte Carlo tool for organ dose estimation in computed tomography

Camille Adrien, Cindy Le Loirec, S. Dreuil, jean-marc bordy

► **To cite this version:**

Camille Adrien, Cindy Le Loirec, S. Dreuil, jean-marc bordy. A new Monte Carlo tool for organ dose estimation in computed tomography. Radioprotection, In press, 55 (2), pp.123-134. 10.1051/radiopro/2020006 . cea-03038511

**HAL Id: cea-03038511**

**<https://cea.hal.science/cea-03038511>**

Submitted on 1 Oct 2021

**HAL** is a multi-disciplinary open access archive for the deposit and dissemination of scientific research documents, whether they are published or not. The documents may come from teaching and research institutions in France or abroad, or from public or private research centers.

L'archive ouverte pluridisciplinaire **HAL**, est destinée au dépôt et à la diffusion de documents scientifiques de niveau recherche, publiés ou non, émanant des établissements d'enseignement et de recherche français ou étrangers, des laboratoires publics ou privés.

# A new Monte Carlo tool for organ dose estimation in Computed Tomography

Camille Adrien<sup>1</sup>, Cindy Le Loirec<sup>1\*</sup>, Serge Dreuil<sup>2</sup>, Jean-Marc Bordy<sup>1</sup>

<sup>1</sup> CEA, List, PC 181, CEA-Saclay 91191 Gif-sur-Yvette Cedex, France

<sup>2</sup> Service de physique médicale, Gustave Roussy, 94805 Villejuif, France

\* Cindy.LELOIREC@cea.fr

## **Abstract (200 words):**

The constant increase of computed tomography (CT) exams and their major contribution to the collective dose led to international concerns regarding patient dose in CT imaging. Efforts were made to manage radiation dose in CT, mostly with the use of the CT dose index (CTDI). However CTDI does not give access to organ dose information, while Monte Carlo (MC) simulation can provide it if detailed information of the patient anatomy and the source are available.

In this work the X-ray source and the geometry of the GE VCT Lightspeed 64 were modelled, based both on the manufacturer technical note and some experimental data. Simulated dose values were compared with measurements performed in homogeneous conditions with a pencil chamber and then in CIRS ATOM anthropomorphic phantom using both optically stimulated luminescence dosimeters (OSLD) for point doses and XR-QA Gafchromic® films for relative dose maps. Organ doses were ultimately estimated in the ICRP 110 numerical female phantom and compared to data reported in the literature.

Comparison of measured and simulated values show that our tool can be used for a patient specific and organ dose oriented radiation protection tool in CT medical imaging.

**Keywords:** Monte Carlo Simulation, Computed Tomography, Organ dose

23 1 Introduction

24 Due to the significant rise of computed tomography (CT) exams in the past few years and the  
25 resulting increase of the collective dose (Kalender 2014), patient dose in CT imaging has become  
26 a subject of interest in public health, especially for children (Akhlaghi *et al* 2015, Journy *et al*  
27 2017a, Journy *et al* 2017b, Habib *et al* 2019). Considerable efforts have thus been made these  
28 past few years to manage radiation dose in CT (Coakley *et al* 2010, Amis 2011, Sodickson 2012  
29 and Mayo-Smith *et al* 2014). However CT protocols are still traditionally optimized using the CT  
30 dose index (CTDI), which is not representative of the patient dose (Kalender 2014 and McCollough  
31 *et al* 2011). Patient-specific dose reports, including absorbed dose to organs, should thus be  
32 suitable for individualized protocol optimization. Because absorbed dose to organ cannot be  
33 directly measured, some research groups attempt to adapt the treatment planning system (TPS)  
34 used in radiation therapy for kV x-ray beams dosimetry. For example, Alaei *et al* 2000 investigated  
35 the accuracy of a convolution/superposition TPS for predicting kV beam dosimetry, but they  
36 reported dose discrepancies up to 145% in the region surrounding bone heterogeneities. Others  
37 groups developed specific software based on precomputed Monte Carlo (MC) data, such as CT  
38 imaging<sup>1</sup> (Kalender *et al* 1999) and ImPact<sup>2</sup>. Axial or helical protocols are included in these  
39 software, but large discrepancies can occur for helical acquisitions, since doses are approximated  
40 from contiguous axial scan. Instead of approximating dose from precomputed MC data, other  
41 research groups developed their own MC software to directly estimate organ dose using  
42 computational patient models or patient DICOM images as inputs.

43 Most of the time, code benchmarking was performed using either a CTDI phantom  
44 (Jarry *et al* 2003, De Marco *et al* 2005 and Deak *et al* 2008) or a custom-designed cylindrical

---

<sup>1</sup><http://ct-imaging.de/en/ct-software-e/impactdose-e.html>

<sup>2</sup><http://www.impactscan.org/>

45 phantom which enables dose measurements at seven different radial distances from its central  
46 axis (Li *et al* 2011). That approach has some limitations because standard and custom-made  
47 phantoms are made of PMMA and only permit dose measurements at selected distances from the  
48 central axis. Impact of heterogeneities and 2D dose gradients cannot be estimated with such  
49 phantoms. Due to the limitations of validation in homogeneous conditions, benchmark in  
50 anthropomorphic conditions is mandatory. For that purpose, DeMarco *et al* 2005 put MOSFET  
51 detectors on the surface of a male anthropomorphic phantom, while Deak *et al* 2008, as well as  
52 Li *et al* 2011, choose to insert TLD (ThermoLuminescent Dosimeter) chips into Alderson-Rando  
53 phantom.

54 In this work we present the dosimetric validation of a MC tool based on PENELOPE  
55 (Sempau *et al* 2003) by comparing simulated and experimental dose estimations. Without any  
56 detailed information provided by the manufacturer, the CT scanner was first modelled only using  
57 information provided by the manufacturer technical note and the method proposed by  
58 Turner *et al* 2009. In a first step the model has been validated in homogeneous conditions by  
59 comparing experimental and simulated integrated dose obtained with a pencil chamber. Simulated  
60 and measured CTDI values have also been compared. Then point dose measurements in an  
61 anthropomorphic phantom, using optically stimulated luminescence detectors (OSLD), were  
62 compared with simulated dose values. Dose distributions in the phantom were also measured with  
63 Gafchromic XR-QA2 films and compared with the simulated dose distributions to validate the  
64 calculated dose gradient in anthropomorphic conditions.

65 Although anthropomorphic validations are mandatory, they require a detector with weak energy  
66 dependence and an accurate calibration for the energy spectra involved in CT. Such conditions  
67 are not met nowadays with ionization chamber used in CT. Calibrations are usually performed for  
68 one normalized spectrum with uncertainties higher than 3-5% and without any correction factor  
69 for other beam qualities. Therefore, given the high number of parameters influencing the

70 measurements and their high uncertainties (about 10% for device parameters such as mAs), 20%-  
71 differences between simulated and measured results are generally considered as a good  
72 approximation of the real situation and were chosen in the present study as the success criterion.  
73 Finally, as an application case of the tool, we estimated organ doses with a numerical  
74 anthropomorphic phantom.

## 75 2 Monte Carlo simulation

### 76 2.1 CT scanner

77 The VCT Lightspeed 64 CT scanner (GE Healthcare, Waukesha, WI) is a third-generation  
78 scanner. As specified in the technical note, focal spot to isocentre distance is 541 mm. Target is  
79 a tungsten-rhenium alloy with a 7 degree tilt angle regarding to reference axis. Dual focal spots  
80 are used depending on current and voltage values. According to IEC 60336, small focal spot is  
81 0.7 mm x 0.6 mm and large focal spot is 0.9 mm x 0.9 mm. The beam full width at half maximum  
82 (FWHM) is adapted as a function of the focal spot size and the chosen aperture. For a 40 mm  
83 beam aperture, the FWHM are 42.6 and 42.9 mm for the small and the large focal spots,  
84 respectively. Use of bowtie filter is related to a maximum Scan Field of View (SFOV). The  
85 maximum SFOV is 32 cm for the small bowtie filter reported as “Ped Body” and 50 cm for the large  
86 bowtie filter reported as “Large Body”. Two tube potentials (100 and 120 kVp), two bowtie filters  
87 (“Ped Body” and “Large Body”) and a 40 mm beam collimation are modelled and presented in this  
88 work.

### 89 2.2 CT model

90 The 2006 release of the MC code PENELOPE (Sempau *et al* 2003) is used to model the VCT  
91 Lightspeed 64 CT scanner (GE Healthcare, Waukesha, WI).

92 For MC simulations, all elements of the X-ray tube need to be modelled. Without any detailed  
93 information provided by the manufacturer, filtration elements are modelled by adapting the

94 experimental method described by Turner *et al* 2009. Based on an initial soft spectrum and  
 95 experimental data, this method provides information on equivalent inherent filtration and  
 96 equivalent bowtie filter shapes, which reproduce the attenuation of the real filtration elements.  
 97 These filtration elements are reported in table 1. For the bowtie filter only the central filtration is  
 98 indicated but the complete equivalent shape is taken into account in the simulation.

99

**Table 1: Filtration of the studied beams.**

Potential (kVp)	SFOV (cm)	Total filtration (inherent + central bowtie filtration).
100	50	5.20 mm Al
120		4.65 mm Al
100	32	3.44 mm Al
120		2.89 mm Al

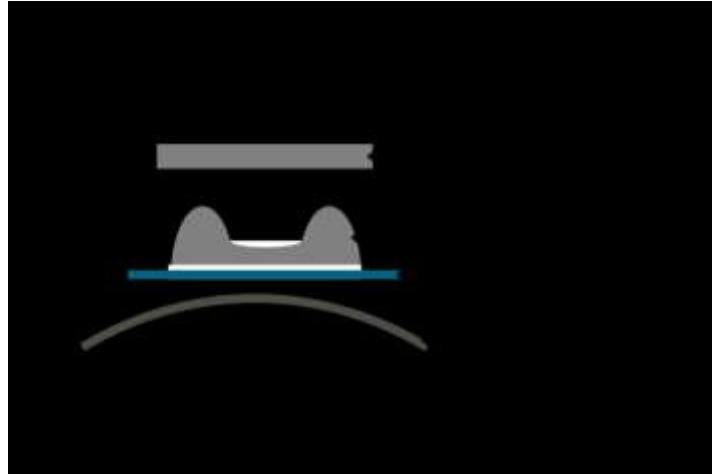
100 One of the specificities of CT scanner is the tube motion of the gantry during the acquisition. Both  
 101 scanning modes, axial and helical, associated with a specific tube path, has to be carefully  
 102 implemented into the MC tool. For that purpose a specific source is defined. Instead of using a  
 103 direct sampling of particles along the tube path and a limited particle splitting (Li *et al* 2011), it was  
 104 taken advantage of the symmetries in geometry to implement a pipe shaped source with two  
 105 variance reduction techniques: a circular splitting and a translational one.

106 The different elements of the X-ray tube are modeled with PENELOPE according to the  
 107 manufacturer technical note<sup>3</sup> and to Turner method (Turner *et al* 2009) for the filtration. A PSF is  
 108 created below the bowtie filter at 15 cm from the focal spot (figure 1). This PSF contains all the

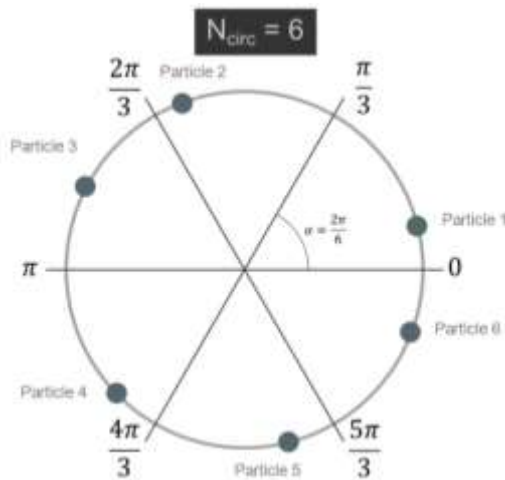
---

<sup>3</sup>LightSpeed™ VCT - Technical Reference Manual

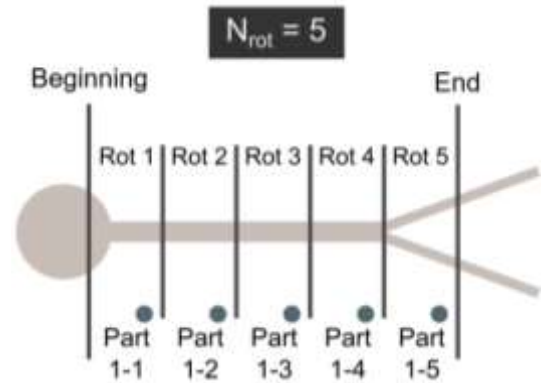
109 relevant information required to perform the simulation: position, direction, energy, statistical  
 110 weight, particle type. Each stored particle is read, split and released for simulation.



(a) CT scanner head and PSF position



(b) Circular splitting



(c) Longitudinal splitting

111 **Figure 1: Information about the CT geometry (a), the PSF location (a), the circular splitting (b) and the**  
 112 **longitudinal splitting (c).**

113 For the circular splitting, the initial particle is splitted in  $N_C$  particles. Each splitted particle is  
 114 sampled on an arc of circle by a random angle ( $\varphi$ ) in the interval  $[2\pi \times i/N_C : 2\pi \times (i + 1)/N_C]$

115 with  $i$  between 0 and  $(N_C-1)$ . User can define  $N_C$  knowing that a large  $N_C$  improves the statistics  
116 but increases the computation time and might introduce bias in the simulation results. For both  
117 scanning modes  $X$  and  $Y$  particle coordinates are modified, with  $X$  and  $Y$  axes the transverse and  
118 vertical directions, respectively. In axial mode simulation, the  $Z$  coordinate remains unchanged.  
119 On the contrary, for helical acquisition, the  $Z$  coordinate is modified according to equation 1:

$$120 \quad z' = z + \varphi/2\pi \times pitch \times collimation \text{ (equ. 1)}$$

121 Once the circular splitting is realized, each particle is splitted a second time in  $N_R$  particles for the  
122 translational splitting. The  $N_R$  value is determined according to the acquisition parameters as:

$$123 \quad N_R = \frac{\text{total explored length}}{\text{pitch} \times \text{collimation}} \text{ (equ. 2)}$$

124 so that it allows a complete covering of the scanning range along the  $Z$  axis. The new  $Z$  coordinate  
125 is then determined according to equation 3, placing each  $N_R$  particle on a gantry rotation.

$$126 \quad z'' = z' + i \times pitch \times collimation \text{ with } i \in [0, N_R] \text{ (equ. 3)}$$

127 Due to the lack of information regarding the tube starting position, which is known to largely  
128 influence dose results (Zhang *et al* 2009), a unique tube path cannot be determined. Choosing  
129 only one tube path can undeniably lead to a dose underestimation/overestimation for some  
130 peripheral organs if the real tube motion is largely different of the simulated path. Because a dose  
131 underestimation cannot be considered as this tool is designed for radiation protection purposes,  
132 choice is made to simulate every possible path. In such a way dose is systematically  
133 overestimated because all peripheral organs will “see” the tube along its path. Tube starting angle  
134 is thus randomly chosen for each initial particle.

### 135 2.3 Analysis of MC data

136 The tube loading information is used to normalize MC results. The tube loading can be related to  
137 a number of emitted electrons ( $N_e$ ) according to equation 4, where  $l$  represents the CT scanning

138 current expressed in Ampere,  $t$  the acquisition time expressed in second, and  $e$  the electron  
 139 elementary charge expressed in Coulomb.

140 
$$N_e = \frac{I(A) \times t(s)}{e} \text{ (equ. 4)}$$

141 Emitted primary electrons are actually related to the simulated primary showers in the MC  
 142 simulation.

143 **2.3.1 Deposited energy in a volume**

144 To validate the MC model in homogeneous conditions a RadCal 10X6-3CT pencil chamber (RTI  
 145 electronics) is used and modeled as a 10 cm length cylinder. The cylinder radius is the one  
 146 reported in the chamber documentation. The parameters used for the simulations are reported in  
 147 table 2. Elastic-scattering parameters  $C_1$  and  $C_2$  are set to 0.05 to have simulations with the  
 148 highest precision. Values of the cut-off energies  $W_{CC}$  and  $W_{CR}$  are fixed at 100 eV. Absorption  
 149 energies of 100 keV for electrons and positrons is compatible with the volume of detection as the  
 150 range of a 100 keV electron is about 0.15 mm in water.

151 **Table 2: MC simulation parameters used for the homogeneous acquisitions.**

Material	$E_{abs,e^-}$ (eV)	$E_{abs,photons}$ (eV)	$E_{abs,e^+}$ (eV)	$C_1$	$C_2$	$W_{CC}$ (eV)	$W_{CR}$ (eV)
Air	$10^3$	$10^2$	$10^4$	0.05	0.05	$10^2$	$10^2$
PMMA	$10^3$	$10^2$	$10^4$	0.05	0.05	$10^2$	$10^2$

152 To simulate acquisitions realized with this pencil chamber, integrated dose in the pencil beam is  
 153 estimated as :

154 
$$DI = \frac{E \times I \times t \times L}{\rho_{air} \times V \times 10^{-3}} \text{ (equ. 5)}$$

155 with  $DI$  the integrated dose (in Gy.cm),  $E$  the mean deposited energy (in eV/shower) obtained with  
 156 the MC simulation in the volume represented the pencil chamber,  $I$  the scanning current (in A),  $t$   
 157 the acquisition time (in s),  $L$  the chamber length (in cm),  $\rho_{air}$  the air density (in g/cm<sup>3</sup>) and  $V$  the  
 158 chamber volume (in cm<sup>3</sup>).

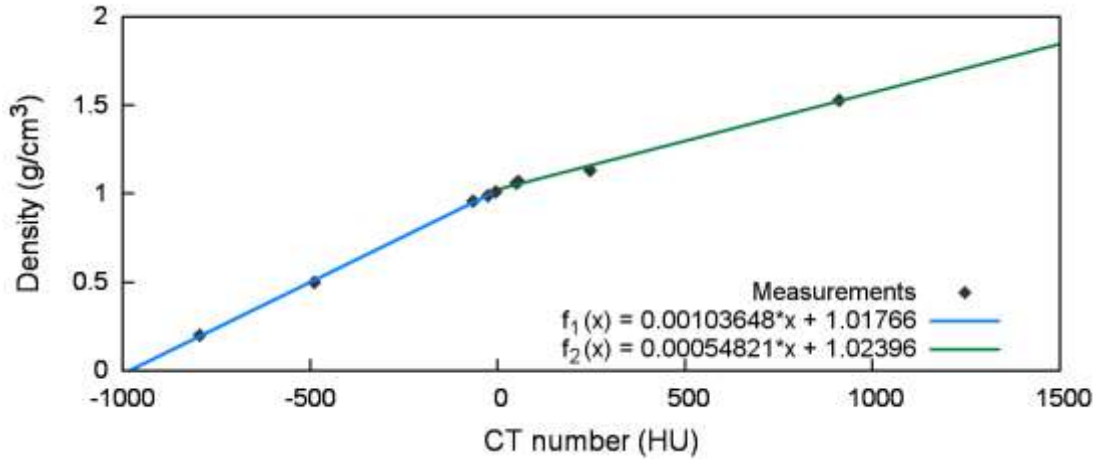
159 Uncertainty on the estimated  $DI$  is evaluated combining the contributions to the uncertainty budget  
 160 using the so called “sandwich law” described in the guide to the expression of uncertainty in  
 161 measurement (ISO/IEC Guide 98-3:2008):

$$\begin{aligned}
 162 \quad u_c^2(DI) &= \left( \frac{I \times t \times L}{\rho_{air} \times V \times 10^{-3}} \right)^2 \times u^2(E) + \left( \frac{E \times t \times L}{\rho_{air} \times V \times 10^{-3}} \right)^2 \times u^2(I) \\
 163 \quad &+ \left( \frac{E \times I \times L}{\rho_{air} \times V \times 10^{-3}} \right)^2 \times u^2(t) + \left( \frac{E \times I \times t}{\rho_{air} \times V \times 10^{-3}} \right)^2 \times u^2(L) \\
 164 \quad &+ \left( \frac{E \times I \times t \times L}{\rho_{air} \times V^2 \times 10^{-3}} \right)^2 \times u^2(V) \text{ (equ. 6)}
 \end{aligned}$$

165 The values of the uncertainties  $u(E)$ ,  $u(I)$ ,  $u(t)$ ,  $u(L)$  and  $u(V)$  are detailed in paragraph 2.3.3.

### 166 2.3.2 Mean dose deposited in a volume

167 For each CT acquisition with the anthropomorphic phantom, the DICOM images of the CIRS  
 168 phantom are converted by associating to each Hounsfield Number a MC material. This conversion  
 169 is done by using a calibration function determined with the CIRS Electron density phantom. The  
 170 calibration function is reported in figure 2. Only four materials are considered here: air, bone, soft  
 171 tissue and lung.



172

173

**Figure 2: Calibration function for the DICOM images of the CIRS phantom.**

174 For point doses comparison, the values obtained in the voxels corresponding to inserts containing  
 175 OSL are compared to measurements.

176 For dose maps comparison, the values obtained in the pixels of the slices corresponding to the  
 177 film position are compared to measurements. To do that, dose maps from film read-outs and from  
 178 MC simulations are centered. As pixel size is not the same between experimental dose map  
 179 (0.51 mm) and MC simulations (2.9 mm) normalized dose profiles are plotted to compare the  
 180 results.

181 To improve the MC computation time for X-ray dosimetric purposes, secondary electrons are not  
 182 tracked if their range is smaller than the considered voxel size (Deak *et al* 2008 and Li *et al* 2011).

183 The effects of this approximation have already been investigated in detail by Chao *et al* 2001, who  
 184 showed negligible differences between incorporating and omitting secondary electrons transport  
 185 for diagnostic energy beams. The parameters used for the simulation respect this assumption.

186 They are reported in table 3 for each material.

187 **Table 3: Parameters used for PENELOPE simulations and for each biological material used in this study.**

Material	$E_{abs,e^-}$ (eV)	$E_{abs,photons}$ (eV)	$E_{abs,e^+}$ (eV)	C1	C2	$W_{CC}$ (eV)	$W_{CR}$ (eV)
----------	--------------------	------------------------	--------------------	----	----	---------------	---------------

Air	$2 \cdot 10^5$	$10^2$	$2 \cdot 10^5$	0.05	0.05	$10^2$	$10^2$
Lung	$2 \cdot 10^5$	$10^2$	$2 \cdot 10^5$	0.05	0.05	$10^2$	$10^2$
Soft tissue	$2 \cdot 10^5$	$10^2$	$2 \cdot 10^5$	0.05	0.05	$10^2$	$10^2$
Bone	$2 \cdot 10^5$	$10^2$	$2 \cdot 10^5$	0.05	0.05	$10^2$	$10^2$

188 To validate the MC model in the anthropomorphic phantom, the mean dose in a voxel has to be  
 189 estimated as:

190 
$$D = D_{MC} \times I \times t \times 1000 \text{ (equ. 7)}$$

191 with  $D$  the dose in the voxel (in Gy),  $D_{MC}$  the estimated MC dose value (in eV/g/shower),  $I$  the  
 192 scanning current (in A) and  $t$  the acquisition time (in s).

193 Uncertainty on the estimated  $D$  is also evaluated combining the contributions to the uncertainty  
 194 budget using the so called “sandwich law” described in the guide to the expression of uncertainty  
 195 in measurement:

196 
$$u_c^2(D) = u^2(D_{MC}) \times (I \times t \times 1000)^2 + u^2(I) \times (D_{MC} \times t \times 1000)^2$$
  
 197 
$$+ u^2(t) \times (D_{MC} \times I \times 1000)^2 \text{ (equ. 8)}$$

198 The values of the uncertainties  $u(D_{MC})$ ,  $u(I)$  and  $u(t)$  are detailed in paragraph 2.3.3.

199 **2.3.3 Uncertainty budget**

200 The stochastic uncertainties  $u(E)$  and  $u(D_{MC})$  due to MC simulation vary for each simulation. It is  
 201 given with a coverage factor  $k = 3$ . Uncertainty of the current ( $u(I)$ ) and the acquisition time ( $u(t)$ )  
 202 are given in the technical note of the CT :

203 
$$u(I) = \bar{\Gamma}(10\% + 0.5 \text{ mA}) \text{ (equ. 9)}$$

204 
$$u(t) = \bar{\Gamma}(5\% + 10\text{ms}) \text{ (equ. 10)}$$

205 However, the confidence interval associated with these uncertainties is not specified. According  
206 to the recommendations of the guide for the expression of measurement uncertainty, we decided  
207 to consider that the uncertainties were expressed for a confidence interval of  $k = 1$  and that the  
208 variable follows a uniform probability law. No information about  $u(V)$  and  $u(L)$  are given. According  
209 to the accuracy needed to build such ionization chamber, we assume that these uncertainties can  
210 be considered as negligible.

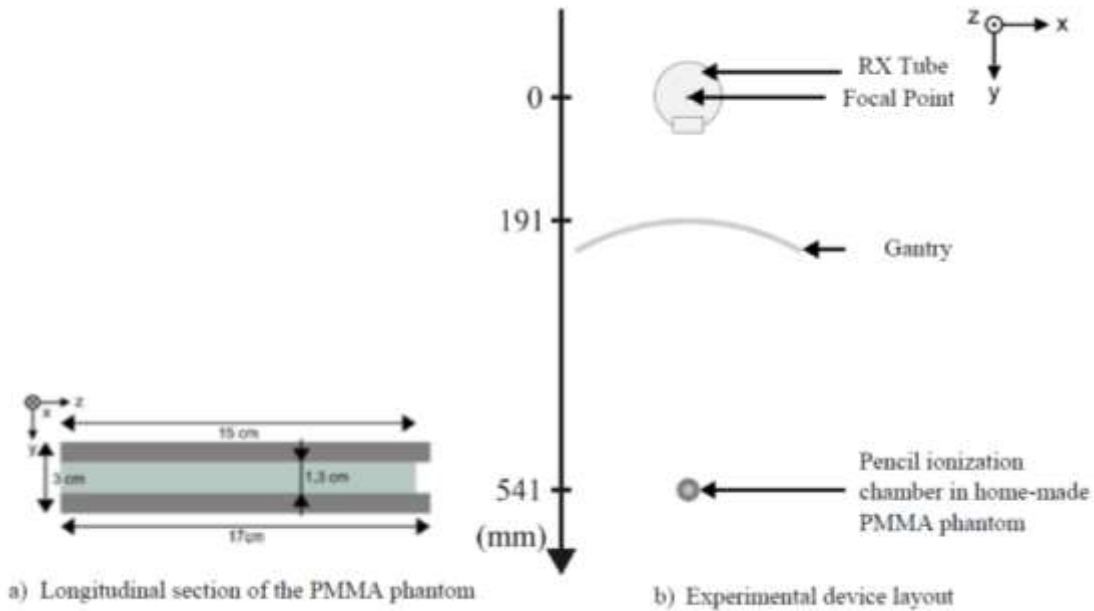
211 Uncertainties are combined with the same confidence interval. In the following they are presented  
212 at  $k=2$ , ie with a confidence interval of  $\approx 95\%$ .

213 It is also considered that all the variables are independent that is to say that the covariance are  
214 not taken into account, this can lead to overestimate the uncertainties. It is assume that this  
215 overestimate is not large.

### 216 3 Model validation in homogeneous conditions

#### 217 3.1 Isocenter validation

218 Integral of the air kerma over 100 mm is measured with a 10X6-3CT Radcal pencil ionization  
219 chamber (figure 3a). The chamber is introduced into a home-made PMMA tube of 3 cm exterior  
220 diameter. Acquisitions have been performed at 100 kVp and 120 kVp, with both bowtie filters, a  
221 40 mm nominal collimation, a 50 cm beam length, 300 mAs and the X-ray tube positioned at the  
222 top of the gantry (figure 3b).



223

224 **Figure 3: Longitudinal section of the PMMA phantom (a) and experimental set-up diagram (b).**

225 3.2 “Air kerma” index validation

226 “Air kerma” index is a dose metric of the CT which represents the amount of radiations emitted  
 227 per rotation of the RX tube. To determine “air kerma” index, two cylindrical phantoms (figure 4)  
 228 composed of one central inserts and 4 peripheral inserts are used:

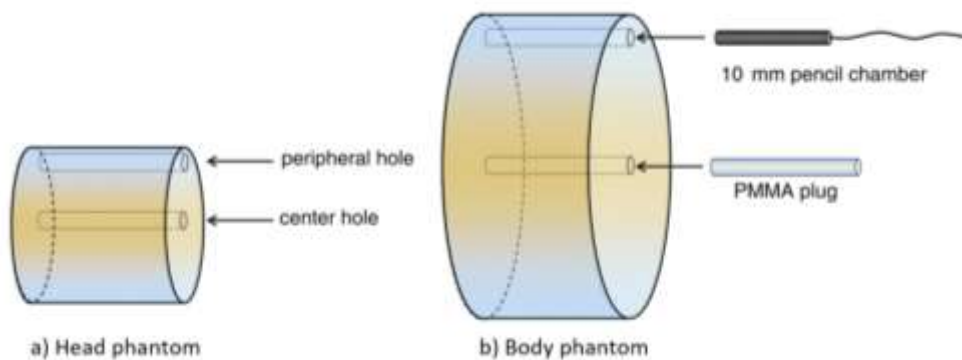
- 229 • The “head phantom” (figure 4a) has a diameter of 16 cm. It is used to calculate the air  
 230 kerma index for head and children CT acquisitions.
- 231 • The “body phantom” (figure 4b) has a diameter of 32 cm. It is used to determine the air  
 232 kerma index for body CT acquisitions

233 The air kerma index  $CTDI_W$  (for Weighting Computed Tomographic Dose Index) is defined as:

234 
$$CTDI_W = \frac{1}{3} (C_{PMMA,100,c} + 2 \times C_{PMMA,100,p}) \text{ (equ. 11)}$$

235 with  $C_{PMMA,100,c}$  being the value of the air kerma index obtained when the pencil chamber is  
236 localized in the central location and  $C_{PMMA,100,p}$  being the mean value of the air kerma index when  
237 the pencil chamber is inserted in the 4 peripheral locations.

238 Acquisitions have been performed at 100 kVp and 120 kVp and for a 40 mm nominal collimation.  
239 The bowtie filter corresponding to the phantom has been used, thus the Ped Body filter for the  
240 head phantom and the Large Body filter for the body phantom. All acquisitions have been  
241 performed with the Radcal pencil chamber, 600 mA and an acquisition time of 1 s. The phantom  
242 is positioned at the CT isocenter. The pencil chamber is positioned in one of the insert while the  
243 other inserts are filled with PMMA cylinders. Five acquisitions are needed to get the air kerma  
244 index in the 5 inserts of each phantom.



245

246 **Figure 4: Layout of the head (a) and body (b) phantoms used for measuring  $CTDI_w$ .**

### 247 3.3 Uncertainty budget

248 Measurements uncertainties are evaluated from information reported in the AIEA report 457 about  
249 the dosimetric practice in diagnostic imaging (IAEA-TRS 457). Scenario 1 has been chosen to  
250 estimate the uncertainty budget. In this scenario, the device is used in conformity with the CEI  
251 61674 norm. According to the data reported in the AIEA report and to the fact that the pencil  
252 chamber is inserted in a PPMA phantom, experimental results are presented with a relative  
253 uncertainty of 13.3%.

254 4 Model validation in clinical conditions

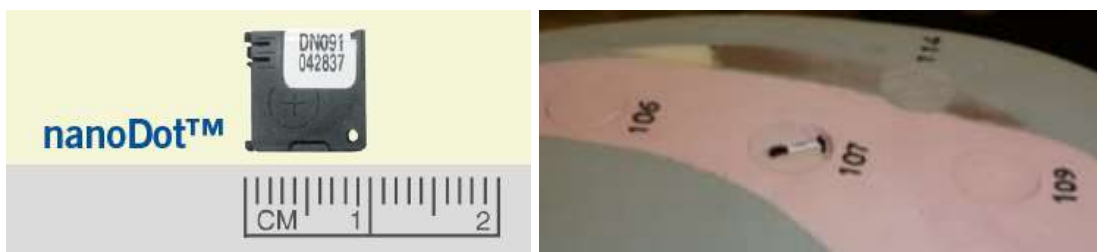
255 Several acquisitions (table 4) are performed combining different parameters (high voltage, pitch,  
256 SFOV).

257 **Table 4: Acquisitions performed experimentally and with the MC simulation to estimate point dose**  
258 **values.**

kVp	Bowtie filter	Pitch	mAs
100	Large	0.984	570
		1.375	750
	Ped	0.516	95
120	Ped	0.984	150

259 4.1 CIRS anthropomorphic phantom

260 The ATOM adult female phantom from CIRS is used to perform measurements with Optically  
261 Stimulated Luminescence dosimeters (OSLDs). This phantom has slots in different localizations  
262 and tissues to insert OSLDs (figure 5). In table 5 are reported the positions of the inserts in which  
263 OSLDs have been inserted for both acquisitions (head and thorax).



264  
265 **Figure 5: Photo of an OSLD on the left and photo of an OSLD inserted in a CIRS phantom slot on the**  
266 **right.**

**Table 5: OSLD locations in the anthropomorphic phantom for thorax and head acquisitions.**

	<b>Location</b>	<b>Tissue</b>	<b>Section</b>	<b>Position</b>
<b>Thorax</b>	Stomach	Soft tissue	21	137
	Right Lung	Lung	20	107
	Spine	Bone	19	102
	Heart	Soft tissue	16	83
	Rib	Bone	15	69
<b>Head</b>	Brain	Soft tissue	3	6
	Skull	Bone	3	10
	Mandible	Bone	7	18
	Thyroid	Soft tissue	10	28

#### 269 4.2 OSL dose assessment

270 In their review, Yukihiro and McKeever 2008, show the possibility of using OSLD for CT  
 271 dosimetry. The great advantages of these detectors is their uniformity in sensitivity because the  
 272 Al<sub>2</sub>O<sub>3</sub>:C powder used in the production process is a homogenized mixture of different crystal  
 273 growth runs. The NanoDot™ (Landauer Inc.) contain single circular OSLD (5.0 mm in diameter)  
 274 placed in an adapter. An effective depth of 0.1 g/cm<sup>3</sup> is assumed as the point of measurement.  
 275 Yukihiro and McKeever mention the OSLD energy dependence, showing variations between 20  
 276 and 30% for potentials ranging from 80 to 140 kVp. We have thus developed a specific user guide  
 277 to take into account this energy dependence.

278 4.2.1 Detector calibration

279 The read-out is performed with the semi-automatic reader MicroStar™ NanoDot™ system.  
280 Depending on the dose level, two light intensities are possible: for low doses (<200 mGy) all 38  
281 LEDs are used and for high doses only 6 LEDs are used. For our application, the reader is always  
282 used in the low dose regime.

283 A calibration of our own OSLD has been carried out on a range from 0 to 150 mGy. Five radiation  
284 qualities (<sup>137</sup>Cs source, <sup>60</sup>Co source, RQR 4, RQR 6 and RQR 9 (NF EN 61267 Norm)), available  
285 at the French national metrological laboratory (Laboratoire national Henri Becquerel, LNHB), are  
286 used. Five detectors have been irradiated for each air kerma value. Average OSLD readings are  
287 used to calculate the calibration factor for each beam quality, assuming that OSLD response is  
288 linear in terms of air kerma. Results are reported in table 6.

289 **Table 6: Calibration function (OSLD reading as a function of air kerma) obtained for the different beam**  
290 **qualities.**

Beam quality	Calibration function
RQR 4	$R = 6781.4 \times K_a + 2475.5$
RQR 6	$R = 6210.6 \times K_a + 2528.5$
RQR 9	$R = 5551.5 \times K_a + 2647.1$
<sup>137</sup> Cs	$R = 2007.6 \times K_a + 2573.1$
<sup>60</sup> Co	$R = 1949.6 \times K_a + 2531.6$

291 4.2.2 Detector read-out analysis

292 Irradiated OSLD, used for measurement, as well as non-irradiated OSLD, are read three times.  
293 Mean reading values for irradiated ( $\bar{r}_I$ ) and non-irradiated OSLD ( $\bar{r}_{NI}$ ) are then computed. These  
294 mean raw reading values are then corrected individually from the OSLD sensitivity (*se*) to obtain

295 the real reading value for irradiated ( $\overline{R_I}$ ) and non-irradiated ( $\overline{R_{NI}}$ ) OSLD, respectively. Finally, the  
 296 corrected signal S, used to determine the dose absorbed by the OSLD is calculated by subtracting  
 297 raw reading values for irradiated ( $\overline{R_I}$ ) and non-irradiated ( $\overline{R_{NI}}$ ) OSLD.

298 To take into account the energy dependence of the OSL detectors, protocol detailed in  
 299 Bordy *et al* 2013 is adapted. The energy spectrum corresponding to the OSL position is  
 300 determined by MC simulation. Calibration factors for each energy bins are convolved using the  
 301 energy spectrum as weight to adapt the calibration factor to the spectrum at the point of  
 302 measurement. Assuming the electronic equilibrium condition are fulfilled, the dose in the tissue is  
 303 obtained by multiplying the air kerma by the ratio of the interaction coefficients:

$$304 \quad D_{medium\ m,Q} = K_{air,Q0} \times \left(\frac{\mu}{\rho}\right)_{Q0,air}^{Q,m} \quad (equ. 12)$$

$$305 \quad \text{with } \left(\frac{\mu}{\rho}\right)_{Q0,air}^{Q,m} = \frac{\left(\frac{\mu_{en}}{\rho}\right)_{Q,m}}{\left(\frac{\mu_{tr}}{\rho}\right)_{Q0,air}}$$

#### 306 4.2.3 Uncertainty budget

307 For each step of the OSLD read-out an uncertainty budget is calculated. At the end, the uncertainty  
 308 associated to the absorbed dose ( $D$ ) in the medium is defined as:

$$309 \quad U_D^2 = U_K^2 \left[ \left(\frac{\mu}{\rho}\right)_{Q0,air}^{Q,m} \right]^2 + U_{(\mu_{en}/\rho)_{Q,m}}^2 \left[ \frac{K}{\left(\frac{\mu_{tr}}{\rho}\right)_{Q0,air}} \right]^2 + U_{(\mu_{tr}/\rho)_{Q0,air}}^2 \left[ \frac{K \times \left(\frac{\mu_{en}}{\rho}\right)_{Q,m}}{\left(\frac{\mu_{tr}}{\rho}\right)_{Q0,air}^2} \right]^2 \quad (equ. 13)$$

310 with  $U_K$  the uncertainty associated to the air kerma and defined as :

$$311 \quad U_K = \left(\frac{1}{a_Q}\right)^2 \times U_S^2 + \left(\frac{-S}{a_Q^2}\right)^2 \times U_{a_Q}^2 \quad (equ. 14)$$

312 where  $U_{aQ}$  is the uncertainty associated to  $a_Q$  the slope of the calibration function corresponding  
313 to the energy spectrum observed at the point of measurement and defined as :

314 
$$U_{aQ}^2 = \left( \frac{1}{\sum_i N_i \times E_i} \right)^2 \sum_i (N_i \times E_i \times U_{a(E_i)})^2 \text{ (equ. 15)}$$

315 and  $U_S$  is the uncertainty associated to the OSLD read-out :

316 
$$U_S^2 = U_{R_I}^2 + U_{R_{NI}}^2 \text{ (equ. 16)}$$

317 with  $U_{R_I}$  being the uncertainty associated to the irradiated detectors and  $U_{R_{NI}}$  being the uncertainty  
318 associated to the non-irradiated detectors ; both of them are calculated thanks to the following  
319 equation :

320 
$$U_{R}^2 = \left( \frac{1}{se} \right)^2 \times U + \left( \frac{U_{\bar{r}}}{se \times se} \right)^2 \times U_{se}^2 \text{ (equ. 17)}$$

321 The uncertainty on the mass interaction coefficients is taken equal to 1%, according to the NIST  
322 (<https://www.nist.gov/>).

#### 323 4.3 Dose maps assessment with XR-QA films

324 When exposed to radiation, the organic based dye of radiochromic films changes color due to  
325 polymerization: the color of XR-QA films turns from orange to brownish-black depending on the  
326 level of exposure (see figure 6). Several features of these detectors have attracted the attention  
327 of the medical physics community: insensitivity to visible light, self-developing characteristics,  
328 dose-rate independence.



329

330 **Figure 6: Film read-out for the head acquisition: the color of XR-QA films turns from orange to**  
331 **brownish-black.**

332 Rampodo *et al* 2006 studied the dependence of XR-QA films for kilovolt energies and they  
333 proposed a method to use these films (reading, calibration, uncertainties assessment). They also  
334 highlighted a variation of the film response with beam energy which can go up to 20%. Boivin *et*  
335 *al* 2011 proposed also to use the films for *in vivo* dosimetry purposes in medical imaging. More  
336 recently, Tomic *et al* 2014 proposed a method for calibrating and correcting the film reading. They  
337 showed that the use of a single calibration function leads to a relative uncertainty of 14% on the  
338 dose values, if the calibration function is obtained for a beam quality taken in the middle of the  
339 investigated energy range. In the following we have considered this value for the uncertainty  
340 associated to the film analysis.

#### 341 4.3.1 Film calibration

342 The films calibration has been carried out in the LM2S (Laboratoire Modélisation, Systèmes et  
343 Simulation) laboratory for a 120 kVp X-ray beam with a HVL of 7.14 mm aluminum. Films and a  
344 Farmer 30013 PTW ionization chamber have been irradiated at the same time in order to  
345 determine the air kerma associated to the film read-out. The Farmer chamber has been previously  
346 calibrated at the French national laboratory of metrology (LNHB) in terms of air kerma. Films are  
347 read before and one week after irradiation and saved as TIF files. Unirradiated film reading is also

348 necessary to obtain net optical density. It is also recommended to control time between irradiation  
349 and read-out (at least 24 h). By using only the red channel, the mean pixel values before ( $PV_{NI}$ )  
350 and after ( $PV_I$ ) irradiation are calculated in a mean 1 mm<sup>2</sup> region of interest. The net optical density  
351 is then defined in equation 17:

$$352 \quad netOD = \log_{10} \left( \frac{PV_{NI}}{PV_I} \right) \text{ (equ. 18)}$$

353 The calibration function linking the air kerma and the netOD has been adjusted according the  
354 following polynomial function (equation 18):

$$355 \quad K_{air,Q0} = a \times netOD + b \times netOD^4 \text{ (equ. 19)}$$

356 As for OSLD the dose in the tissue is obtained by multiplying the air kerma by the ratio of the mass  
357 interaction coefficients.

#### 358 4.3.2 Film analysis

359 Gafchromic XR-QA2 films are irradiated to study the dose gradient. Films are cut to fit the  
360 anatomical shapes of the female anthropomorphic phantom and placed between two phantom  
361 slices. For thorax acquisitions, films cannot be inserted into the breasts of the phantom because  
362 breast are made from a single piece without any insert or slice. Stencil of the films contours are  
363 used to ensure the reproducibility of the film positioning during the reading steps before and after  
364 irradiation. For all acquisitions, the tube speed is fixed at 0.7 s/rot and the films are read four times  
365 before and one week after the irradiation. Films are read several times to ensure that film storage  
366 and handling have been performed in good conditions (dry and dark environment, no dust or  
367 fingerprints ..). Optical density values are then converted into air kerma according to the calibration  
368 function.

369 A thoracic and a head acquisition (table 7) have been performed.

370 **Table 7: Acquisitions performed experimentally and with the MC simulation to estimate dose maps.**

<b>kVp</b>	<b>Bowtie filter</b>	<b>Pitch</b>	<b>Position in the phantom</b>
100	Large	0.516	Between section 16 and 17
120	Ped	1.375	Between section 7 and 8

371 5 Organ dose estimation

372 Organ doses for a thoracic localisation have then been estimated into the female phantom  
373 provided in ICRP Publication 110. Simulations are performed for the Large Body bowtie filter with  
374 a 50 cm SFOV, 100 and 120 kVp, a 40 mm collimation adapted to the used focal spot (42.6 and  
375 42.9 mm), three mAs (100, 200 and 300), a 0.7 s/rot tube speed and three pitch values (0.531 –  
376 0.969 – 1.375). Dose values to each voxel across all the voxels belonging to each organ are  
377 averaged. According to the organ  $w_T$  factors reported in the ICRP 103, we decid to report the dose  
378 absorbed by the more sensitive organs thus the left breast glandular tissue, the stomach wall, the  
379 left pulmonary tissue, the esophagus and the spinal cord.

380 6 Comparison of experimental and simulated results

381 To compare experimental results ( $r_{exp}, \sigma_{exp}$ ) and MC estimation ( $r_{MC}, \sigma_{MC}$ ) we have used 2 index :

- 382 • the deviation defined as :

383 
$$dev = \frac{r_{MC} - r_{exp}}{r_{exp}} \times 100 \text{ (equ. 21)}$$

- 384 • and the overlap defined as :

385

$$ovlp = 100 \times e^{-\frac{(r_{MC}-r_{exp})^2}{2(\sigma_{rMC}^2+\sigma_{exp}^2)}} \text{ (equ. 22)}$$

386 7 Results387 7.1 Isocenter experimental validation

388 Table 8 shows the measured and simulated integral of the air kerma over 100 mm. Results show  
 389 a good agreement between the simulations and the measurements with a deviation less than 10%  
 390 and an overlap larger than 87% for the 4 cases considered here.

391 **Table 8: Measured and simulated values obtained for the integral of the air kerma in the pencil**  
 392 **chamber.**

			MC estimation	Experimental value	Comparison	
			$DI \pm U_{DI}$ (mGy.cm)		<i>dev</i> (%)	<i>ovlp</i> (%)
Ped Bowie filter	Body	100 kV	289.9 ± 35.1	278.6 ± 18.4	4.0	96.0
		120 kV	400.6 ± 48.4	408.2 ± 26.9	-1.9	99.1
Large Bowie filter	Body	100 kV	206.7 ± 25.5	216.1 ± 14.3	-4.4	94.9
		120 kV	309.1 ± 37.8	331.4 ± 21.9	-6.7	87.8

393

394 7.2 Validation of the air kerma index estimation

395 Table 9 shows the measured and simulated integral of the air kerma index obtained with both  
 396 phantoms. Results show a good agreement between the simulations and the measurements with  
 397 a deviation less than 4% and an overlap larger than 89% for the 4 cases considered here.

398

399

400

401

402

**Table 9: Measured and simulated air kerma index obtained with both phantoms.**

			MC estimation	Experimental value	Comparison	
			$CTDI_w \pm U_{CW}$ (mGy)		<i>dev</i> (%)	<i>ovlp</i> (%)
Ped Bowie filter	Body	100 kV	$76.3 \pm 4.4$	$74.2 \pm 4.9$	2.8	95.0
		120 kV	$112.9 \pm 6.4$	$117.6 \pm 7.8$	-4.0	89.4
Large Bowie filter	Body	100 kV	$37.7 \pm 2.6$	$36.5 \pm 2.4$	3.2	94.7
		120 kV	$58.7 \pm 4.0$	$59.0 \pm 3.9$	-0.5	99.8

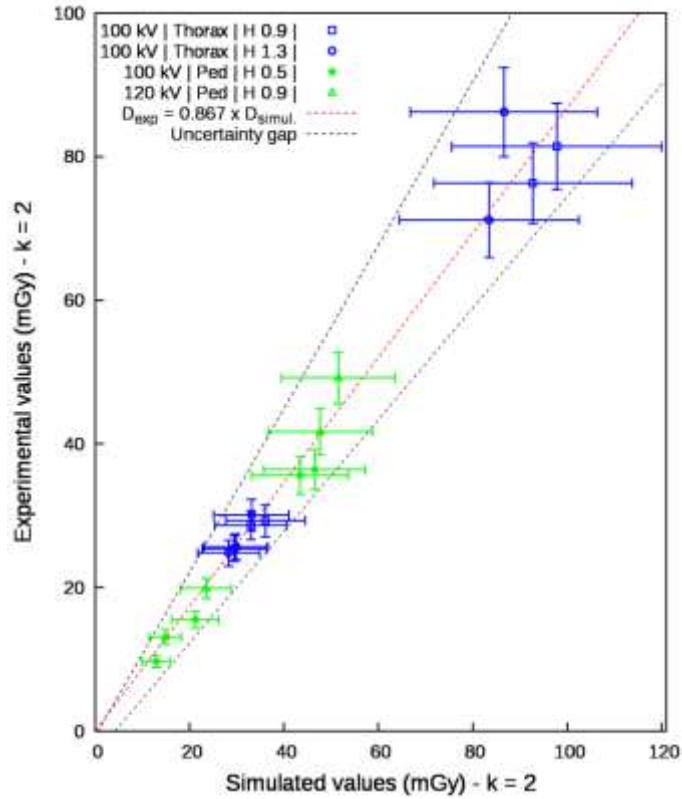
403

404     7.3   Point dose comparison

405   Experimental and simulated dose values are reported in figure 7 as well as the relation between  
406   them:

$$407 \quad D_{exp} = 0.867 \times D_{simul} \text{ (equ. 23)}$$

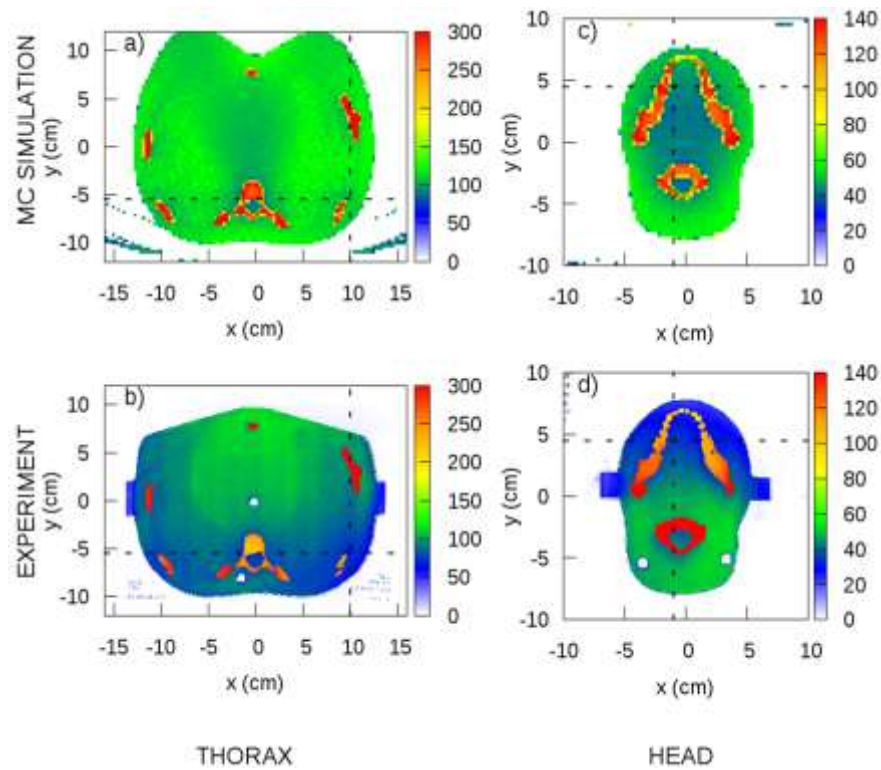
408   Simulated values are on average higher than the experimental ones. The uncertainty bars plotted  
409   in figure 7 is obtained by fitting the MC uncertainty associated to each simulated values. This one  
410   is about 23.2% (k=2) for all the simulations performed here. The experimental uncertainty is about  
411   7.4%.



412  
 413 **Figure 7: Experimental dose values versus simulated dose values and uncertainties given at k=2 for the**  
 414 **head (in green) and thorax (in blue) acquisitions with the female ATOM phantom. The relation**  
 415 **between both dose values are fitted (in red) as well as the uncertainty gap (in black).**

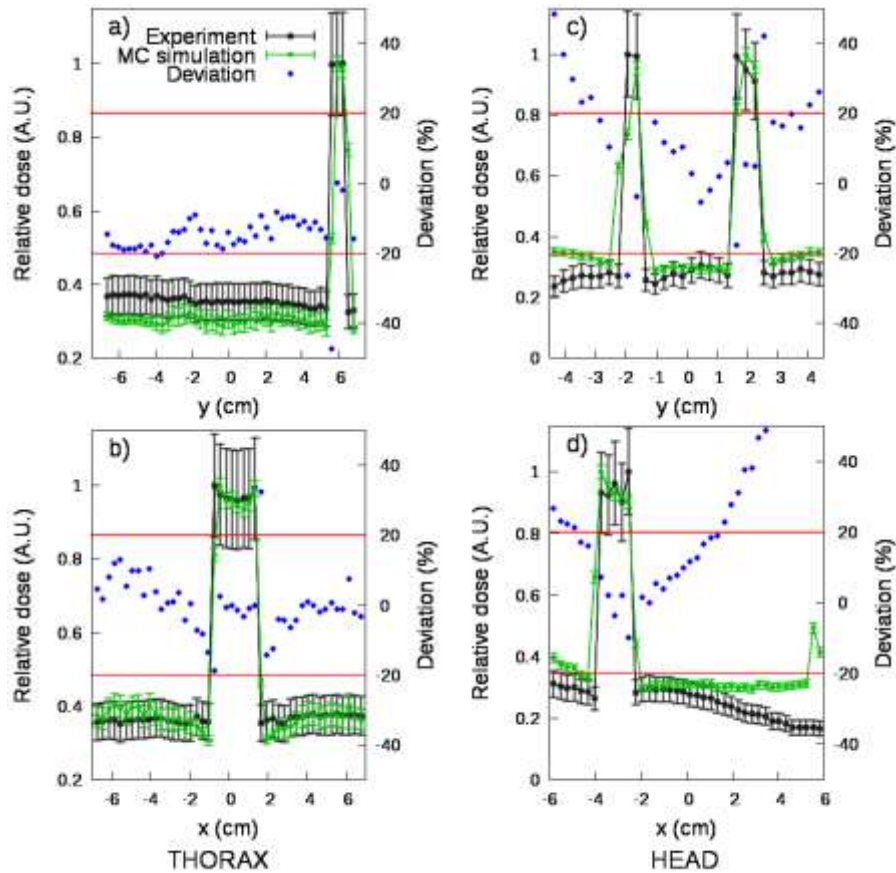
416 7.4 Dose maps comparison

417 Experimental and simulated dose distributions for a head scan are reported in figure 8. Large  
 418 differences can be observed between the two maps and will be discussed later in the discussion  
 419 section.



420  
 421 **Figure 8: Simulated and measured dose distributions in mGy for a head (c and d) and a thorax (a and b)**  
 422 **scan. Dashed lines indicate the profiles used for figure 9.**  
 423

424 Validation of the dose gradient is performed by comparing simulated and experimental profiles  
 425 reported in figure 9 and obtained from figures 8a, 8b, 8c and 8d. In figures 8 and 9 the MC  
 426 uncertainty is about 3% and the experimental uncertainty about 15%. Deviations between  
 427 simulations and experiments are less than 20% in bone heterogeneities. In soft tissue regions the  
 428 deviation can be higher, especially for the head acquisition. This deviation is mainly due to the  
 429 path of the x-ray tube during the experimental scan which is not simulated accurately in the MC  
 430 simulation, the initial position of the tube being experimentally unavailable.



431  
 432 **Figure 9: Simulated and measured relative dose profiles for the head (c and d) and the thorax (a and b)**  
 433 **acquisitions. The profiles are obtained for the dashed lines reported in figure 8. The deviation between**  
 434 **simulation and measurement is reported in blue.**

435 7.5 Organ dose estimation

436 Organ doses for the Large Body Bowtie filter, 120 kVp, 40 mm collimation, 1.375 pitch and  
 437 100 mAs, are reported in table 10 and compared with Zhang *et al* 2012 results, who also estimated  
 438 organ dose for the female phantom described in the ICRP 110. They simulated in details the GE  
 439 VCT LightSpeed 64 thanks to accurate data provided by the manufacturer. They used a modified  
 440 version of PENELOPE reported in Li *et al* 2011 to estimate organ doses in the ICRP 110 phantoms.  
 441 Our results, obtained in less than one hour in 24 CPU for all cases, are a little bit larger than the  
 442 dose values reported by Zhang *et al* 2012. Deviations are less than 5.8% for the four organs  
 443 considered here.

444 **Table 10: Comparison of organ doses for a thoracic helical acquisition obtained with our MC tool and**  
 445 **reported by Zhang *et al* 2012.**

Organs	Simulated organ doses (mGy)		
			Deviations(%)
	This study	Zhang <i>et al</i> 2012	
Esophagus	9.8 (0.003)	9.3	5.4
Lung	10.9 (0.003)	10.3	5.8
Breast	10.2 (0.002)	10.1	1.0
Stomach	11.1 (0.001)	10.9	1.8

446

447 8 Discussion and Conclusion

448 Despite a lack of information about the scanner geometry, the GE VCT LightSpeed 64 has been  
 449 modelled by adapting the method developed by Turner *et al* 2009.

450 Results obtained in homogeneous conditions validate the use of the MC model for dosimetric  
 451 estimation. Measured and simulated integrals of the air kerma over 100 mm are in agreement;  
 452 this also validates the use of the tube load information to convert simulated results into Gray. By  
 453 comparing integral of the air kerma in table 8 and their associated uncertainties, we note that the  
 454 simulation uncertainties budget is actually deteriorated by the conversion factor contribution.  
 455 According to the manufacturer technical note, current and acquisition time have 10% and 5%  
 456 uncertainty on the displayed value, respectively. Despite these values, relative uncertainties are  
 457 below 15%. Such uncertainties are compatible with medical imaging applications.

458 Measured and simulated point dose obtained in anthropomorphic conditions show deviations up  
459 to 15%. However confidence intervals are overlapped allowing us to conclude that results are in  
460 agreement. The uncertainty budget for simulated doses is mainly by the conversion factor  
461 uncertainties. The relative uncertainties for the tube current and the acquisition time are  
462 respectively 10% and 5% at  $k=1$ , as reported in the technical note. Simulated dose uncertainties  
463 might seem quite large (about 22% at  $k=2$ ), but such uncertainties are compatible with dosimetric  
464 purposes in medical imaging. The benefit of the conversion factor is therefore maintained.

465 Large differences in the simulated and the experimental dose distributions can be noted. All the  
466 experimental dose maps show an important effect of the initial tube position, as already reported  
467 by several authors (Li *et al* 2011 and Zhang *et al* 2009). The surface dose distribution resulting  
468 from a helical acquisition is periodic (Dixon and Ballard 2007) and the tube start angle determines  
469 the location of the high and low dose regions. It has been reported by (Zhang *et al* 2009) that the  
470 magnitude of organ dose reduction resulting from varying tube start angle varies from 10 to 30%  
471 depending on the location and size of the organs. In the experimental dose distribution, shown in  
472 figures 8b and 8d, the tube position relative to the phantom slice containing the film can be easily  
473 determined, since a higher dose is delivered to the top and the back of the phantom for the thorax  
474 and the head acquisition, respectively. However, the tube path relative to the patient cannot be  
475 fully worked out because the tube starting angle information is not provided on the GE VCT  
476 Lightspeed 64 scanner. Taking into account this lack of information it has been decided to  
477 randomly sample the tube starting angle for each simulated particle. By making this choice, all  
478 possible tube paths are simulated, leading to a more homogenous dose distribution (figures 8a  
479 and 8c) and an overestimation for some location of the real delivered dose. Nevertheless, instead  
480 of underestimating the dose for radiosensitive organs the MC simulation considers the worst case  
481 and provides the maximum dose which could be delivered.

482 For directly irradiated areas there are sometimes some differences in the vicinity of bone  
483 structures. They are mainly due to the different pixel sizes between the film and the dose matrices.  
484 Due to the small number of particles, the size of the voxels in the dose matrix cannot match the  
485 size of that of the film. Indeed, the smaller the size of the voxels, the more one has to increase the  
486 number of particles to converge the simulation.

487 In addition to the difficulties related to the difference in resolution, the dose maps from the  
488 simulation highlight problems related to voxelization of the phantom. Since the voxels are larger  
489 than those used for the phantom, a voxel in the dose grid can be composed of several tissues  
490 (lung, bone and soft tissue in our case). If a voxel is composed of several tissues, it can be  
491 considered as being composed of an hybrid tissue associated with an intermediate density  
492 according to the densities of the materials initially present and their density. The dose deposit is  
493 then affected and the separation between the tissues is less marked. However, the dose profiles  
494 show that the gradients are still well respected.

495 Besides, in their article Long *et al* 2013 showed from MC simulations that the starting angle could  
496 lead to organ dose differences between -20% and 34% compared to the average value. We also  
497 found such discrepancies when comparing simulations and measurements obtained with OSLD.  
498 By combining the information of Long's article and the non-homogeneous dose deposit visible on  
499 the films due to the random draw of the starting position, the important differences found in the  
500 comparison between measurement and simulation for the OSLDs can be explained.

501 For one studied case, organ dose estimations with our software are in agreement with those  
502 published by Zhang *et al* 2012, attesting the reliability of the developed software. Organ dose  
503 estimation in the ICRP 110 phantoms can be thus performed in a short notice, less than one hour  
504 using 24 CPU. In the future, improvements would be considered to reduce the simulation time.

505

506 9 Acknowledgments

507 The authors thank warmly Helena Chesneau for the calibration of the Gafchromic films and Fabien  
508 Moignau, Marc Denoziere, Nelly Lecerf, for their help in the calibration of the OSLD.

509 10 References

510 Akhlaghi P., Miri-Hakimabad H. and Rafat-Motavalli L. (2015) Dose estimation in reference and  
511 non-reference pediatric patients undergoing computed tomography examinations: a Monte Carlo  
512 study, *Radioprotection* **50**, 43-54.

513 Alaei P., Gerbi B. J. and Geise R. A. (2000) Evaluation of a model-based treatment planning  
514 system for dose computations in the kilovoltage energy range, *Med. Phys.* **27**, 2821-2826.

515 Amis E. S. (2011) CT Radiation Dose; Trending in the Right Direction, *Radiology* **261**, 5-8.

516 Boivin J., Tomic N., Fadallah B., DeBlois F., and Devic S. (2011) Reference dosimetry during  
517 diagnostic CT examination using XR-QA radiochromic film model, *Med. Phys.* **38**, 5119-5129.

518 Bordy J.M., Bessieres I., d'Agostino E., Domingo C., d'Errico F., di Fulvio A., Knezevic Z., Miljanic  
519 S., Olko P., Ostrowsky A., Poumaredé B., Sorel S., Stolarczyk L., Vermesse D.(2013)  
520 Radiotherapy out-of-field dosimetry: experimental and computational results for photons in a water  
521 tank *Radiat. Meas.* **57**, 29–34.

522 Chao T. C., Bozkurt A., and Xu X. G. (2001) Conversion coefficients based on the VIP-Man  
523 anatomical model and EGS4, *Health Phys.* **81**, 163–183.

524 Coakley F.V., Gould R., Yeh B. M., and Arenson R.L. (2010) CT Radiation Dose: What can you  
525 do right now in your practice?, *AJR* **196**, 619-625.

526 Deak P., van Straten M., Shrimpton P.C., Zankl M. and Kalender W.A. (2008) Validation of a Monte  
527 Carlo tool for patient specific dose simulations in multi-slice computed tomography, *Eur. Radiol.*  
528 **18**, 759-772.

529 De Marco J.J., Cagnon C.H., Cody D.D., Stevens D.M., Mc Collough C.H., O'Daniel J. and McNitt-  
530 Gray M.F. (2005) A Monte Carlo based method to estimate radiation dose from multidetector CT  
531 (MDCT): Cylindrical and anthropomorphic phantoms, *Phys. Med. Biol.* **50**, 3989-4004.

532 Dixon R.L. and Ballard A.C. (2007) Experimental validation of a versatile system of CT dosimetry  
533 using a conventional ion chamber: Beyond CTDI [sub 100] *Med. Phys.* **34**, 3399–3413.

534 IAEA. Technical Reports Series n° 457 (2007) Dosimetry in Diagnostic Radiology: An International  
535 Code of Practice.

536 ICRP Publication 103 (2007) The 2007 recommendations of the International Commission on  
537 Radiological Protection, *Ann. ICRP* **37**, 1-332, Pergamon Press.

538 ICRP Publication 110 (2009) Adult Reference Computational Phantoms, *Ann. ICRP* **39**, 1-162,  
539 Elsevier.

540 ISO/IEC Guide 98-3 (2008) Uncertainty of measurement – Part 3: Guide to the expression of  
541 uncertainty in measurement (GUM:1995), *Joint Committee for Guides in Metrology*, JCGM 100.

542 Habib Geryes B. , Hornbeck A., Jarrige V., Pierrat N., Ducou Le Pointe H., Dreuil S. (2019) Patient  
543 dose evaluation in computed tomography: A French national study based on clinical indications,  
544 *Physica Medica* **61**,18-27.

545 Hubbell J.H. and Seltzer S.M. (2009) Tables of x-ray mass attenuation coefficients and mass  
546 energy-absorption coefficients from 1 keV to 20 MeV for elements Z =1 to 92 and 48 additional  
547 substances of dosimetric interest, available at: <http://www.nist.gov/pml/data/xraycoef/index.cfm>

548 Jarry G., DeMarco J.J., Beifuss U., Cagnon C.H. and McNittGray M.F. (2003) A Monte Carlo based  
549 method to estimate radiation dose from spiral CT: from phantom testing to patient specific models,  
550 *Phys. Med. Biol.* **48**, 2645-2663.

551 Journy N.M.Y., Lee C., Harbron R. W., McHugh K., Pearce M. S. and Berrington de Gonzales A.  
552 (2017a) Projected cancer risks potentially related to past, current, and future practices in  
553 paediatric CT in the United Kingdom 1990-2020, *British Journal of Cancer* **116**, 109-116.

554 Journy N. M. Y., Dreuil S., Boddaert N., Chateil J.-F., Defez D., Ducou-le-Pointe H., Garcier J.-M.,  
555 Guersen J., Habib Geryes B., Jahnen A., Lee C., Payen-de-la-Garanderie J., Pracros J.-P.,  
556 Sirinelli D., Thierry-chef I. and Bernier M.-O. (2017b) Individual radiation exposure from computed  
557 tomography: a survey of paediatric practice in French university hospitals, 2010-2013, *European*  
558 *Radiology* **28**, 1432-1084

559 Kalender W.A., Schmidt B., Zankl M. and Schmidt M. (1999) A PC program for estimating organ  
560 dose and effective dose values in computed tomography *Eur. Radiol.* **9**, 555 – 562.

561 Kalender W.A. (2014) Dose in x-ray computed tomography, *Phys. Med. Biol.* **59**, R129-R150.

562 Li X., Segars w.P., Surgeon G.M., Colsher J.G., Toncheva G., Yoshizumi T.T. and Frush D.P.  
563 (2011) Patient-specific radiation dose and cancer risk estimation in CT: Part I. Development and  
564 validation of a Monte Carlo program, *Med. Phys.* **38**, 397 – 407.

565 Long D.I.J., Lee C., Tien C., Fisher R., Hoerner M.R., Hintenlang D. and Boch W. E. (2013) Monte  
566 Carlo simulations of adult and pediatric Computed Tomography exams: Validation studies of organ  
567 doses with physical phantoms, *Med. Phys.* **40**, 013901-1 – 013901-10.

568 Mayo-Smith W.W., Hara A.K., Mahesh M., Sahani D.V., and Pavlicek W. (2014) How I Do It:  
569 Managing Radiation Dose in CT, *Radiology* **273**, 657-672.

570 McCollough C.H., Leng S., Yu L., Cody D.D., Boone J.M., McNitt-Gray M.F. (2011) CT Dose Index  
571 and Patient Dose: They are not the same thing, *Radiology* **259**, 311-316.

572 Rampado O., Garelli E., Deagostini S., and Ropolo R. (2006) Dose and energy dependence of  
573 response of gafchromic XR-QA film for kilovoltage x-ray beams, *Phys. Med. Biol.* **51**, 2871-2881.

574 Sechopoulos I., Ali E.S.M., Badal A., Badano A., Boone J.M., Kyprianou I., Mainegra-Hing E.,  
575 McNitt-Gray M.F., McMillan K.L., Rogers D.W.O., Samei E. and Turner A.C. (2015) Monte Carlo  
576 Reference Data Sets for Imaging Research, *The Report of AAPM Task Group* **195**.

577 Sempau J., Fernandez-Varea J.M., Acosta E., and Salvat F. (2003) Experimental benchmarks of  
578 the Monte Carlo code PENELOPE, *Nucl. Instrum. Methods B* **207**, 107-123.

579 Sodickson S. (2012) Strategies for reducing radiation exposure in multi-detector row CT, *Radiol.*  
580 *Clin. N. Am.* **50**, 1-14.

581 Tomic N., Quintero C., Whiting B.R., Aldelaijan S., Bekerat H., Liang L., DeBlois F., Seuntjens J.,  
582 and Devic S. (2014) Characterization of calibration curves and energy dependence gafchromic  
583 xr-qa2 model based radiochromic film dosimetry system, *Med. Phys.* **41**, 062105.

584 Turner A.C., Zhang D., Kim H.J., De Marco J.J., Cagnon C.H., Angel E., Cody D.D., Stevens D.M.,  
585 Primark A.N., McCollough C.H., McNitt-Gray M.F. (2009) A method to generate equivalent energy  
586 spectra and filtration models based on measurement for multidetector CT Monte Carlo dosimetry  
587 simulations, *Med. Phys.* **36**, 2154-2164.

588 Yukihiro E.G. and McKeever S.W.S. (2008) Optically stimulated luminescence (osl) dosimetry in  
589 medicine, *Phys. Med. Biol.* **53**, R351-R379.

590 Zhang D., Zankl M., DeMarco J.J., Cagnon C.H., Angel E., Turner A.C. and McNitt-Gray M.F.  
591 (2009) Reducing radiation dose to selected organs by selecting the tube start angle in MDCT  
592 helical scans: A Monte Carlo based study, *Med. Phys.* **36**, 5654-5664.

593 Zhang Y., Li X., Segars W., and Samei E. (2012) Organ doses, effective doses, and risk indices  
594 in adult CT: Comparison of four types of reference phantoms across different examination  
595 protocols, *Med. Phys.* **36**, 3404-3423.

596

597

598

599

600

601

602

603

604